Sensing and Bio-Sensing Research 50 (2025) 100900

Contents lists available at ScienceDirect

Sensing and Bio-Sensing Research

journal homepage: www.elsevier.com/locate/sbsr

Development of a semi-quantitative lateral flow immunoassay to classify the levels of SARS-CoV-2 antibodies in plasma

Laura M. Rey Gomez [a], Rena Hirani [a,b], David W. Inglis [c], Andrew Care [d], Yuling Wang [a,*]

[a] School of Natural Sciences, Faculty of Science and Engineering, Macquarie University, Sydney, NSW 2109, Australia
[b] Australian Red Cross Lifeblood, Sydney, NSW 2015, Australia
[c] School of Engineering, Faculty of Science and Engineering, Macquarie University, Sydney, NSW 2109, Australia
[d] School of Life Sciences, University of Technology Sydney, NSW 2007, Australia

ARTICLE INFO

Keywords:
Lateral flow immunoassays
Plasma
SARS-CoV-2
Gold nanoparticles
Semi-quantitative
Antibodies
Serology

ABSTRACT

Lateral flow immunoassays (LFIAs) are versatile paper-based detection devices widely used for rapid on-site biomarker detection, yet they remain largely qualitative, which limits their utility in point-of-care (POC) settings. This study presents a colorimetric, semi-quantitative, and equipment-free LFIA format using a barcode-style design to categorize antibody levels as low, medium, or high. Using anti-SARS-CoV-2 antibodies in human plasma as a model, a multi-line assay was constructed with highly spherical gold nanoparticles (AuNPs) for improved sensitivity. The barcode-style LFIA demonstrated strong agreement with the validation method, with 90 % of results falling within ±1 category of the reference values. Additionally, the impact of AuNP morphology was investigated by comparing the assay performance with highly spherical (S), commercial (C), and quasi-spherical (Q) nanoparticles. While S-AuNPs improved the detection limit by two-fold in spiked plasma samples, all AuNP types performed comparably in clinical plasma. These results demonstrate a promising strategy for bridging the gap between qualitative and quantitative testing in low-resource or POC settings, enabling more informative readouts without the need for instrumentation.

1. Introduction

Analysis of antibody levels in plasma samples may be of value during classification of convalescent plasma for therapeutic treatments. The current "gold standard" for antibody detection include plaque reduction neutralization tests (PRNTs), followed by chemiluminescent immunoassays (CLIAs), and enzyme-linked immunosorbent assays (ELISA) [1–4]. However, these methods can be time-consuming and difficult to implement in low- and middle-income countries due to the need for specialized equipment and trained personnel [5].

Although lateral flow immunoassays (LFIAs) are rapid and portable, they remain largely qualitative, which limits their utility as serological tests for public monitoring. Current efforts to improve LFIA readouts include altering the output from colorimetric to signal based using fluorescence or Raman spectroscopy. Although able to significantly improve sensitivity, the requirement for specific instrumentation and image/signal data processing limits their use in POC settings and low- and middle-income countries [6–8]. Smartphone LFIAs also present a promising approach, but device and software variability often present challenges in data reproducibility and user-friendliness [9,10].

In this study, a colorimetric, equipment-free, and semi-quantitative LFIA was constructed using a multi-line barcode-style design that provides additional information regarding the target concentration in the sample. In view of the recent Coronavirus pandemic (COVID-19), a barcode-LFIA was constructed to detect antibodies against severe acute respiratory syndrome Coronavirus 2 (anti-SARS-CoV-2) in plasma. A qualitative test provides a "yes" or "no" answer where the concentration of the sample could be inferred from the intensity of the test line. However, a semi-quantitative readout has been especially calibrated to match clinically relevant concentrations. It provides information about the sample's concentration as a range defined by the total number of test lines, therefore facilitating interpretation without additional equipment. In the context of COVID-19 antibodies, a concentration range is helpful to identify a person's level of immunity or screen for donations suitable for convalescent plasma treatment. Barcode or ladder style LFIAs have been previously developed for the detection of food toxins, pathogens,

* Corresponding author.
E-mail addresses: laura.reygomez@hdr.mq.edu.au (L.M. Rey Gomez), rhirani@redcrossblood.org.au (R. Hirani), david.inglis@mq.edu.au (D.W. Inglis), andrew.care@uts.edu.au (A. Care), yuling.wang@mq.edu.au (Y. Wang).

https://doi.org/10.1016/j.sbsr.2025.100900
Received 25 August 2025; Received in revised form 15 October 2025; Accepted 21 October 2025
Available online 24 October 2025

and plasma proteins [11–19]. However, this is the first iteration of a barcode-LFIA for the equipment-free detection of antibody levels in plasma.

The level of anti-SARS-CoV-2 antibodies can be interpreted as low, medium, or high by counting the number of test lines colored after 15 min. The level of antibodies, or titer, is a helpful indicator of a person's immunity to a specific pathogen at a certain point in time, which can help in monitoring immune responses, guide immunization decisions and policies, or screen for suitable plasma donations for convalescent plasma therapy [20–22]. Current serological tests are conducted using ELISAs or plaque reduction neutralization tests (PRNTs). These tests are informative and high throughput, but they are time-consuming, costly, and require specific equipment and highly trained personnel. LFIAs are efficient alternatives to rapidly detect the levels of antibody and provide information pertaining to a person's immunity or the suitability of a donation for convalescent plasma treatment. However, while LFIAs excel at their versatility and ease of use, they fall short in sensitivity and specificity [23,24].

Simple ways to improve the sensitivity of LFIAs include adjusting the morphology of gold nanoparticles (AuNPs) [25,26], or making changes to the functionalization reaction to optimize the orientation [27,28] and binding efficiency of bioreceptors [29]. Due to the limitations in LFIA sensitivity, the assay was optimized by assessing the impact of AuNPs morphology on sensitivity by comparing spherical (S), commercial (C) or quasi-spherical (Q) conjugated AuNPs. Highly spherical cetyltrimethylammonium bromide (CTAB)-capped AuNPs were previously observed to significantly improve the limit of detection (LOD) of LFIAs. However, it is still unknown if improvements to LFIA performance can also be obtained from citrate-capped AuNPs synthesized with simpler methods, and if these improvements are also noticeable with complex samples such as plasma. Using citrate-capped AuNPs could provide significant performance improvements without the need for arduous synthesis methods that require more time and material cost. The final barcode-LFIA was constructed and validated with spiked plasma and various clinical samples to fully elucidate the assay performance.

2. Methods

2.1. Materials

Tetrachloroauric (III) acid ($HAuCl_4$), trisodium citrate dihydrate ($Na_3C_6H_5O_7{\cdot}2H_2O$), sodium tetraborate decahydrate ($Na_2B_4O_7{\cdot}10H_2O$), boric acid (H_3BO_3), casein from bovine milk, bovine serum albumin (BSA), phosphate buffered saline (PBS), and 50 nm commercial (C)-AuNPs, and glass fiber diagnostic pad (GFDX20305PK) were purchased from Merck Life Science, Darmstadt, Germany. Tris-base was purchased from Bio-Rad Laboratories, Hercules, USA. Goat anti-Human IgG antibody, sucrose and Tween20 were purchased from ThermoFisher Scientific, Waltham, USA. SARS-CoV-2 Recombinant Spike Protein and anti-SARS-CoV-2 Spike Protein S1 Receptor-Binding Domain IgG monoclonal antibody were purchased from STEMCELL Technologies, Vancouver, Canada. Glass fiber sample pad GFB-R7L, polyester matrix conjugate pad PT-R7, laminated nitrocellulose membranes with wicking rates of 90 s/4 cm (90CNPH) and 200 s/4 cm (200CNPH), and cellulose fiber absorbent pad AP-080 were purchased from MDI Advanced Microdevices, Haryana, India.

2.2. Sample collection and ethics approval

This study was conducted following National Statement on Ethical Conduct in Human Research (2007) guidelines in accordance with the National Health and Medical Research Council Act 1992. Ethics approval was obtained from the Macquarie University Human Research Ethics Committees (approval no. 520211106535637) and Australian Red Cross Lifeblood (Lifeblood) Ethics committee (approval Hirani 22,062,020). Blood donor samples pre- and post the detection of COVID-19 in Australia were obtained from Lifeblood.

Unless stated otherwise, frozen plasma samples were thawed at RT (room temperature) for 10 min and centrifuged (15,000 rpm, 5 min). The supernatant was then heat inactivated by incubating at 56 °C for 30 min. The heat inactivated plasma was used for all analysis.

2.3. Preparation of AuNPs

All glassware was pre-cleaned with Aqua Regia (3 HCl:1 HNO_3). AuNPs were stored at 4 °C for future use.

S-AuNPs (~50 nm) were synthesized according to a previously reported seeded growth procedure [30]. Synthesis was performed inside a fume hood under reflux conditions with a silicon bath and round-bottom two-neck flasks. AuNPs seeds (~17 nm) were first synthesized by boiling 48.5 mL Milli-Q water with stirring (150 °C, 600 rpm), then 0.5 mL 1.0 % *w/v* $HAuCl_4$ was added, and the mixture was left to boil for 10 min. A volume of 1.5 mL 1.0 % w/v sodium citrate buffer was then added and was left to boil for an additional 30 min before removing from the heat. AuNPs (~50 nm) were grown by bringing 45.5 mL of Milli-Q water to a boil and adding 2 mL 100 mM Tris-base. After 5 min, 2 mL AuNP seeds (~17 nm) and 0.5 mL 1.0 % w/v $HAuCl_4$ was added in quick succession, and the solution was incubated for 30 min before removing from heat and storing.

C-AuNPs of 50 nm in diameter were sourced from Merck Millipore in a reactant-free colloid suspension (0.1 mM PBS). According to the data sheet, "the AuNPs may be prepared by reduction of metal salt precursors with reducing agents, such as by citrate reduction of $HAuCl_4$ in water", it is therefore assumed that they were synthesized with citrate-based methods [31].

Q-AuNPs (~50 nm) were synthesized according to a modified Turkevich method [32]. Briefly, 50 mL 0.001 % *w/v* $HAuCl_4$ was brought to a boil with stirring, then 0.75 mL 1.0 % w/v sodium citrate ($Na_3C_6H_5O_7{\cdot}2H_2O$ pH 5) was quickly added. After 10 min, the heating was turned off, and the solution was stirred for another 20 min and left to cool before storing.

2.4. Optimization of AuNP functionalization

Prior to functionalization, the concentration of Spike proteins was optimized for every AuNP type [33–35]. The concentration of all AuNPs was first standardized to optical density (OD) = 1.5–1.6 using UV–visible absorption spectroscopy (UV–vis), then the pH of the system was adjusted to pH 8 with 100 mM borate buffer (100 mM Sodium tetraborate decahydrate, 100 mM Boric acid, pH 9). In a 96-well plate, 200 µL of pH adjusted AuNPs were added in triplicate with Spike protein, diluted in 0.1 mM PBS, to the final concentration of 0, 0.5, 1, 1.5, 2, 2.5 µg/mL. After an incubation period with stirring (20 min, 650 rpm, RT), 20 µL of 10 % NaCl was added, and the mixture was incubated with stirring (20 min, 650 rpm, RT). Finally, the samples were centrifuged (8 min, 5500 rpm, RT) and resuspended in 800 µL 0.1 mM PBS for UV–vis measurements.

The AuNPs surface coverage and conjugate stability were measured by calculating a gold aggregation test (GAT) value from UV–Vis absorbance at the localized surface plasmon resonance (LSPR) peak and at 600 nm, where a greater difference between absorbances indicates lower levels of aggregation, calculated using [34,35]:

$$GAT\ value = (Abs_{LSPR} - Abs_{600})_{Untreated} - (Abs_{LSPR} - Abs_{600})_{After\ NaCl\ addition}$$

The optimal concentration of Spike proteins was determined as the highest concentration to cause a significant change in GAT values, therefore indicating the start of a plateau and a diminishing effect on stability. This concentration was used for every functionalization reaction henceforth.

2.5. Functionalization of AuNPs with spike proteins

A volume of 1.5 mL AuNPs was adjusted to pH 8 by adding 40 μL borate buffer, followed by 3 μL or 4.5 μL of 0.5 mg/mL Spike protein in 0.1 mM PBS. AuNPs were incubated with stirring (20 min, 650 rpm, RT) and blocked with 100 μL of 0.1 % casein, followed by another incubation as described above. The biofunctionalized AuNPs were washed 3 times (5500 rpm, 9 min) and resuspended in 300 μL 1 % BSA, 5 % sucrose, 5 mM PBS.

2.6. Preparation of anti-SARS-CoV-2 LFIA and procedure

LFIA strips consisted of a sample pad, conjugate pad, a nitrocellulose membrane with test (T) and control (Ct) lines, and an absorbent pad all assembled onto a backing card and cut into 3 mm strips with a programmable strip cutter. The T line was coated with 1.75 mg/mL Goat anti-Human IgG antibodies specific to the fragment crystallizable (Fc) region, diluted in 10 mM PBS 1 % ethanol at a rate of 1.0 μL/cm and 50 mm/s speed. The Ct line consisted of 0.5 mg/mL anti-SARS-CoV-2 IgG in 10 mM PBS 1 % ethanol coated at 0.5 μL/cm and 50 mm/s speed. The conjugate pad was prepared by spraying functionalized AuNPs onto a glass fiber pad at 15 μL/cm with 50 mm/s speed. Subsequently, the prepared nitrocellulose membrane and conjugate pad were dried in an incubator at 37 °C for 1 h and stored in a desiccator at 25 % humidity for 24 h prior to LFIA assembly.

The LFIAs were performed by diluting 1 μL inactivated plasma in 50 μL running buffer (1 % BSA, 1 % gelatine, 0.25 % PVP, 10 mM PBS) and adding this mixture to the sample pad. After 15 min, the LFIAs were extracted from the cassettes and scanned using a flatbed scanner.

2.7. Instruments

UV–visible absorption spectroscopy (UV–vis) was performed with a JASCO V-760 Spectrometer (Jasco, Easton, MD USA). Dynamic light scattering (DLS) was measured with the Zetasizer ZS (Malvern Panalytical, Malvern UK) at 25 °C with a 633 nm laser set at 4 mW power output. Surface charge (Zeta potential) was also measured with the Zetasizer ZS in disposable folded capillary cells DTS1070 (Malvern Panalytical) on samples diluted at 1:1 ratio with 0.1 mM PBS. Nanoparticle tracking analysis (NTA, NanoSight NS300, Malvern Panalytical) was performed on samples diluted with Milli-Q water at 1/100 or 1/1000 dilution and measured 3 runs at RT (~21 °C) with a 402 nm blue laser. Transmission electron microscopy (TEM, Phillips CM10) images were taken at 100 kV voltage and magnification of x64,000. Samples were concentrated 3 x or 10 x in Milli-Q water and a 10 μL drop was added to the carbon side of a formvar/carbon film coated with 300 mesh hexagonal copper grid (Nanjing Zhongjingkeyi Technology, Jiangsu, China) and left to settle for 4 min before absorbing with filter paper. This process was repeated 2 more times, and the copper grid was left to dry overnight. LFIA strips were made using the XYZ Platform Dispenser HM3030/HM3035 and cut with the Automatic Strip cutter ZQ2002 (Kinbio Tech., Shanghai, China). Images were obtained with an Epson Perfection V39 flatbed scanner (Officeworks, VIC, Australia).

2.8. Statistical analysis

Image analysis and calculations were performed with ImageJ software version 1.53j to 1.53o (National Institutes of Health (NIH), Bethesda, MD USA), MATLAB version 24.2 R2024b, and R Studio version 4.4.1 [36]. TEM images were processed using particle analysis in ImageJ to measure Feret's diameter. For LFIA strips, scanned images were first cropped with the rotated rectangle tool in ImageJ, then processed in MATLAB by measuring the area under the OD peak (AUP) of the T and Ct lines using the green channel [37,38]. Curve fitting to the four-parameter logistic (4PL) nonlinear model was performed in R Studio [39,40].

The LOD of the concentration was calculated according to CLSI EP17 guidelines [41]. The limit of blank (LOB) was first evaluated as the mean of the signal at blank concentration plus 1.645 times the standard deviation of the blanks ($LOB = mean_{blank} + 1.645(SD_{blanks})$). The LOD of the signal (LOD_S) was calculated as the LOB plus 1.645 times the maximum standard deviation of the 2 lowest concentrations ($LOD_S = LOB + 1.645(SD_{Low})$). The LOD was then solved using the 4PL nonlinear equation given as:

$$LOD_{Signal} = d + \frac{(a-d)}{1 + \left(\frac{LOD_{Concentration}}{c}\right)^{b}}$$

Where a is the lower asymptote of the curve, representing the signal where the concentration approaches 0; b is the slope; c is the inflection point representing the signal at half the concentration, and d is the upper asymptote representing the signal where the concentration plateau.

3. Results and discussion

3.1. LFIA design

The LFIA was designed to detect anti-SARS-CoV-2 IgG antibodies in human plasma (Fig. 1). AuNPs of different morphologies were biofunctionalized with Spike proteins (Fig. 1A), which are found on the surface of the SARS-CoV-2 virus and serve as the first point of interaction with host cells (via angiotensin-converting enzyme 2 (ACE2) receptor) and antibodies [42,43]. Once added to the sample pad, the sample travels to the conjugate pad to encounter the AuNPs bound to Spike proteins. In the presence of anti-SARS-CoV-2 antibodies, a complex with AuNPs is formed and released from the conjugate pad to travel along the nitrocellulose membrane. Since the T lines were coated with Goat anti-Human IgG antibodies against the Fc region, assay specificity will largely depend on the AuNP conjugates, thus allowing for a more direct evaluation of the efficacy of the AuNPs. The AuNPs-Spike protein-antibody complexes will bind the Goat anti-Human IgG antibody to form a red T line (Fig. 1B, Upper panel). If there are no anti-SARS-CoV-2 antibodies in the sample, no complexes are formed with AuNPs, and a T line does not emerge (Fig. 1B, Lower panel). The Ct line was coated with commercially sourced anti-SARS-CoV-2 antibodies, which bind to free AuNPs via the Spike protein on the surface.

3.2. Synthesis and characterization of AuNPs with different morphologies

S-AuNPs were synthesized using a seed-growth method, wherein smaller nanoparticles act as seeds that are grown to the desired size [30]. Q-AuNPs were synthesized using the conventional Turkevich method [32], and C-AuNPs were synthesized with a proprietary method that is similarly based on the reduction of metal salt precursors (according to the datasheet from the supplier) [32]. These three types of AuNPs were characterized with TEM, UV–vis spectroscopy, DLS, and NTA as shown in Fig. 2. The morphology of all AuNPs can be observed in the TEM images in Fig. 2A-C. It was evident that S-AuNPs (Fig. 2A) presented a more rounded and consistent surface compared to Q-AuNPs (Fig. 2C), which had a noticeable difference between the largest and smaller nanoparticles in the image. C-AuNPs (Fig. 2B) were also consistent in size but presented a more angular surface with sharper corners. AuNP size was measured in ImageJ using the maximum Feret diameter. The mean max. Feret diameter for all AuNPs was ~50 nm with the lowest standard deviation from S-AuNPs (Table 1). It is important to note that the experimental size of C-AuNPs differed from the expected size requested on purchase (54.6 nm vs 50.0 nm). An ellipticity index (length / width) close to 1 indicates a highly spherical object equal in length and width. S-AuNPs and C-AuNPs exhibited shapes with higher sphericity than Q-AuNPs, with the lowest variation obtained from S-AuNPs.

Normalized extinction spectra (Fig. 2D) shows LSPR bands at 525 nm

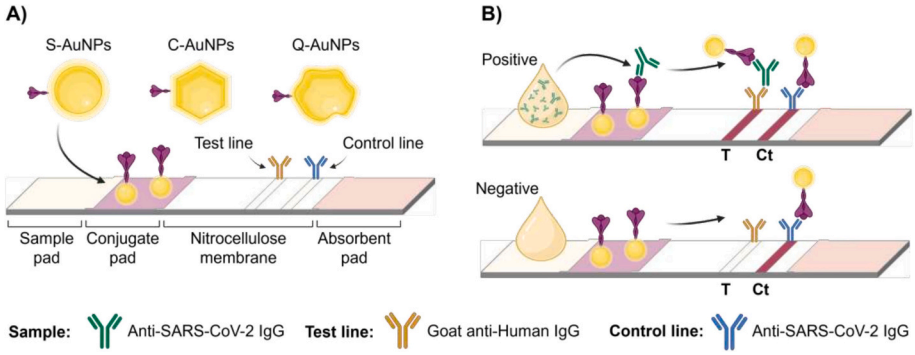

Fig. 1. Schematic diagram of lateral flow immunoassay (LFIA) design. A) shows the three types of gold nanoparticles (AuNPs): spherical (*S*)-AuNPs, commercial (C)-AuNPs and quasi-spherical (Q)-AuNPs that were tested. B) indicates the expected outcomes when a positive (upper panel) or negative sample (lower panel) is applied. (For interpretation of the references to colour in this figure legend, the reader is referred to the web version of this article.)

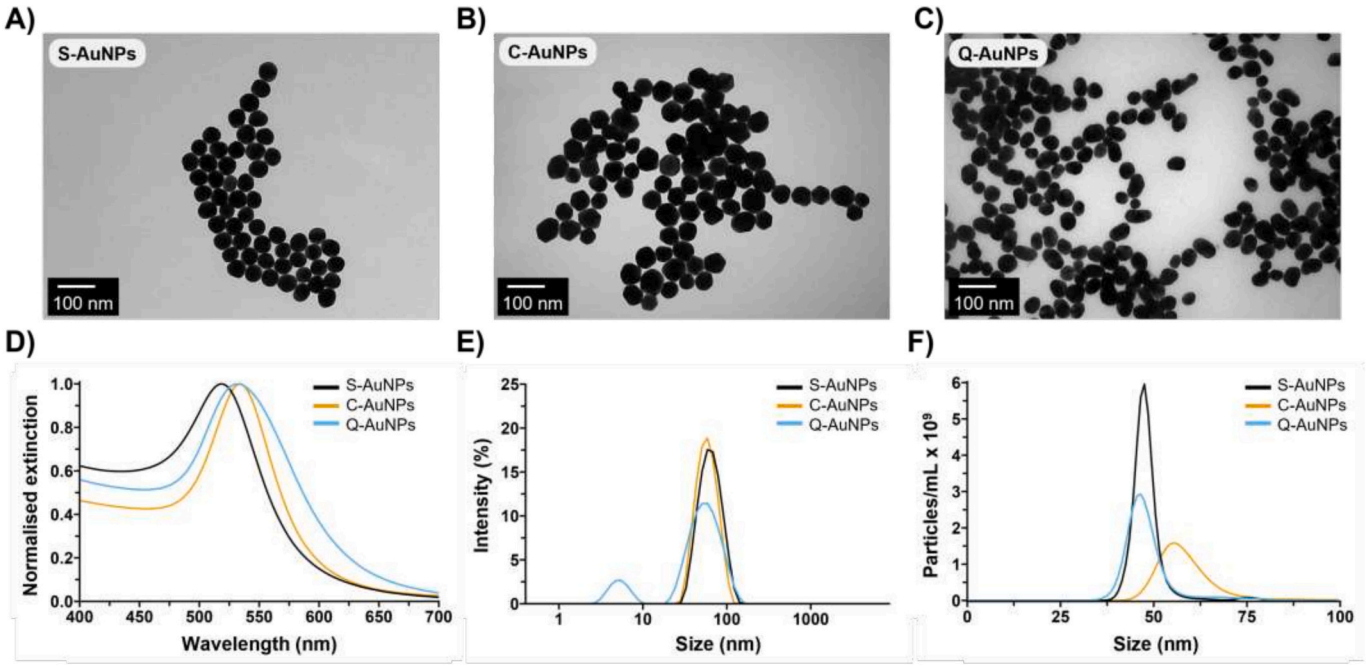

Fig. 2. Characterization of AuNPs. TEM images showing the morphology of A) spherical (*S*)-, B) commercial (C) and C) quasi-spherical (Q) gold nanoparticles (AuNPs) at x64,000 magnification. D) extinction spectra for each particle type. E) Dynamic Light Scattering (DLS) plots for each particle type. F) Nanoparticle tracking analysis (NTA) measurements for each particle type. S-AuNPs (black), C-AuNPs (yellow), and Q-AuNPs (blue). (For interpretation of the references to colour in this figure legend, the reader is referred to the web version of this article.)

Table 1
Summary of geometrical parameters of the different types of AuNPs obtained from TEM measurements.

Sample	Size [nm][a]	SD [%]	Ellipticity index ± SD[b]	n
S-AuNPs	49.1	10.6	1.16 ± 0.18	695
C-AuNPs	54.6	16.4	1.19 ± 0.27	493
Q-AuNPs	51.5	18.0	1.33 ± 0.32	471

[a] Average of maximum Feret diameter.
[b] Max. Feret diameter / Min. Feret diameter ± absolute uncertainty.

for S-AuNPs, 534 nm for C-AuNPs, and 532 nm for Q-AuNPs, which is in accordance with previous literature [30,44]. Fig. S2 shows the raw extinction spectra for all AuNPs. S-AuNPs and C-AuNPs presented narrower LSPR peaks compared Q-AuNPs, indicating a lower size distribution and higher monodispersity. DLS and NTA measurements (Fig. 2E-F) indicated that the average hydrodynamic size of all AuNPs was close to 50 nm with lowest size standard deviation and polydispersity index (PDI) obtained from S-AuNPs (Table S1). A false peak around 5–10 nm was observed for DLS measurements of Q-AuNPs, this is typically observed in strongly scattering non-spherical AuNPs >30 nm in size and serves as additional evidence of the low sphericity of Q-AuNPs [45]. NTA showed that C-AuNPs had slightly larger hydrodynamic size compared to the other AuNPs (~50 nm), which could be indicative of a slightly larger AuNP size or the presence of an undisclosed surface capping agent (Fig. 2F). All AuNPs reported surface charges of < -30 mV, indicating high colloid stability (Table S1). S-AuNPs synthesized with the citrate-based seeded growth method exhibited the highest level of sphericity and size dispersity, followed by C-AuNPs then Q-AuNPs.

3.3. Optimization of AuNPs bioconjugates and LFIA

Passive functionalization of AuNPs relies on electrostatic charges between the AuNPs surface and proteins to drive the initial interactions [27]. Therefore, adjusting the system pH is often necessary to create conditions with favorable charge distribution and stability. As pH 6 and

9 resulted in AuNP aggregation following incubation with Spike proteins, pH 8 was selected for subsequent optimization of the concentration of Spike proteins on the surface of AuNPs (Fig. S1). Since the isoelectric point of the Spike protein RBD/His is ~8.9, at pH 8 the protein is slightly positively charged, which facilitates initial interactions with the negatively charged AuNPs [46].

For optimization, a gold aggregation test (GAT) was conducted where different amounts of Spike protein were tested. NaCl was used to disturb the AuNPs surface charge and induce aggregation, which was prevented if the AuNPs surface was protected by a protein layer. Therefore, the protein concentration that prevented salt-induced aggregation of the AuNPs was considered the optimal amount.

Absorbance was measured at the LSPR peaks (525 nm S-AuNPs, 534 nm C-AuNPs, and 532 nm Q-AuNPs) and at 600 nm, and the differences in these absorbances before and after salt-induced aggregation were calculated [34,35]. The GAT value represents the differences in aggregation levels between AuNP conjugates. The optimal Spike protein concentration can be deduced as the concentration that caused the lowest difference between untreated AuNPs and AuNP conjugates. As shown in Fig. 3, the optimal concentration of Spike proteins was 1 μg/mL for S- and C-AuNPs, and 1.5 μg/mL for Q-AuNPs. This was confirmed through extinction spectra (Fig. S3), hydrodynamic size, and zeta potential (Table S2). A binding efficiency of 99.6 ± 37 % was obtained for S-AuNPs, 86.8 ± 39 % for C-AuNPs, and 95.8 ± 45 % for Q-AuNPs. The binding efficiency was defined as the percentage difference between experimental and theoretical amount of Spike proteins on AuNPs (experimental / theoretical x 100). The relevant calculations and assumptions are discussed in detail in the Supplementary information (Tables S3 and S4).

3.4. Effect of AuNPs morphology on LFIAs

The effect of AuNPs morphology on the sensitivity of LFIAs was studied using LFIAs designed for the detection of human IgG antibodies against SARS-CoV-2 virus. Each AuNP morphology was bioconjugated with the optimal concentration of Spike proteins obtained experimentally (Fig. 3). To evaluate the detection limits of the LFIAs, human plasma collected in early 2019 (prior to the discovery of SARS-CoV-2) was spiked with anti-SARs-CoV-2 IgG antibodies at concentrations 0, 0.125, 0.25, 0.5, 1, and 2 μg/mL. AuNP saturation was reached at concentrations of ≥2 μg/mL, as evidenced by the decreasing intensity of the Ct line in proportion to sample concentration and T line intensity (Fig. 4A). At this point, most AuNPs were bound to IgG from the sample and the amount of available excess AuNPs to bind to the Ct line rapidly diminished. Due to this observation, only the AUP of the T line was used for analysis instead of the T/C ratio commonly used. The AUP was measured using the green channel. Curve fitting was performed with the 4PL nonlinear function, which is widely used with bioassays that exhibit plateaus at high concentrations – as is the case with LFIAs [47,48]. The AUP values were plotted as a function of anti-SARS-CoV-2 IgG antibodies at concentrations ranging from 0 to 2 μg/mL (Fig. 4B). The R^2 values were 0.997 for S-AuNPs, 0.999 for C-AuNPs, and 0.997 for Q-AuNPs. The LOD was calculated to be 56.0 ng/mL for S-AuNPs, 99.1 ng/mL for C-AuNPs, and 107 ng/mL for Q-AuNPs. The LOD obtained from S-AuNPs was roughly 2-fold lower than the other morphologies (1.8× and 1.9×, respectively). These results, in combination with the steeper slope in the S-AuNPs curve, revealed that higher sensitivities could be achieved with slightly more spherical and monodispersed AuNPs even in highly complex media.

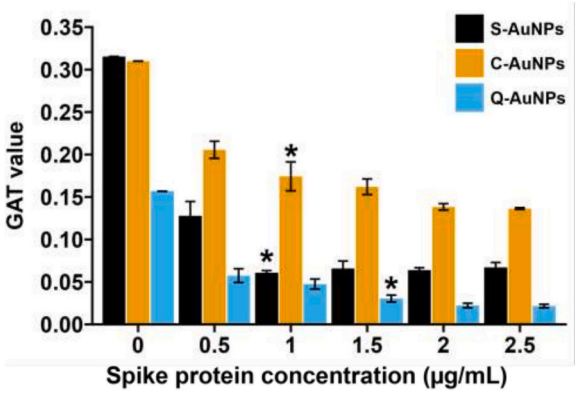

Fig. 3. Functionalization of nanoparticles with Spike proteins and characterization. A) Gold aggregation test (GAT) value describing the differences in salt-induced aggregation between bare gold nanoparticles (AuNPs) and AuNPs functionalized with varying Spike protein concentrations. Conjugates with lower GAT values present lower levels of aggregation and higher stability. The data represent mean ± SD (error bars, $n = 3$). (*) Represents the last point at which a significant difference to the previous concentration was observed ($p < 0.05$, n = 3). (For interpretation of the references to colour in this figure legend, the reader is referred to the web version of this article.)

3.5. LFIA with positive COVID-19 human samples

Human plasma samples with pre-determined levels of anti-SARS-CoV-2 antibodies (as measured by ELISA) [49] were tested with the LFIAs to evaluate the performance of AuNPs when exposed to real-life samples with biological variation. Negative controls (10) consisted of plasma samples collected early in 2019 prior to SARS-CoV-2 detection [50]. Positive samples (10) were collected from Australian blood donors who had provided convalescent donations following exposure to the SARS-CoV-2 virus [49]. Triplicate LFIAs tests were conducted with 1 μL plasma and 50 μL running buffer, after 15 min the images were scanned and analyzed (Fig. 5A-C).

The highest number of true positives was observed from S-AuNPs, followed by C-AuNPs and Q-AuNPs. C-AuNPs presented the lowest number of false positives compared to S-AuNPs and Q-AuNPs. It is possible that false positives observed were caused by reactions with endogenous antibodies in the plasma matrix [51–53]. To test if interferences from plasma matrix play a role in overall intensity, 0.5 μg/mL anti-SARS-CoV-2 antibodies were spiked in 10 mM PBS before adding to the LFIAs (Fig. S4A). A 5-fold increase in T line intensity was observed for S-AuNPs and C-AuNPs, and 7.5-fold increase for Q-AuNPs, suggesting that interference from plasma samples greatly affects the LFIA sensitivity, and that Q-AuNPs might be more susceptible to such interferences than the other AuNP morphologies (Fig. S4B). Fig. S4C shows that the degree of non-specific binding increased when applying 5 μL of clinical negative control samples instead of the 1 μL applied in Fig. 5A-C.

Plasma interference was also observed to affect positive detection as shown in Fig. S4D. Volumes of 1 or 5 μL of a plasma sample – that did not show an increase in non-specific binding in Fig. S4C – were spiked with either 0 ng (as negative control) or 25 ng anti-SARS-CoV-2 IgG (Fig. S4D). The LFIAs showed negative outcomes for negative (0 ng) control samples. However, 5 μL spiked plasma samples were similarly negative to untreated samples, while assays run with 1 μL spiked plasma demonstrated a strong positive band. Notably, there was a reduction in the intensity of the Ct band between 0 ng and 25 ng using 5 μL plasma, which is indicative of interactions between the AuNPs and the spiked antibodies in the sample. The lack of T line intensity could therefore be attributed to interferences from plasma proteins with LFIA bioreceptors, specifically, the Goat anti-Human IgG antibodies on the nitrocellulose membrane possibly binding to other endogenous antibodies in the plasma samples [51–53]. Since 1 μL plasma contained lower levels of interfering proteins and antibodies, T lines were more prominently visible. Although false positives can be mitigated by using 1 μL volumes, further optimization is required to eliminate the occurrence of false positives before translating the proof-of-concept LFIA towards a clinical application.

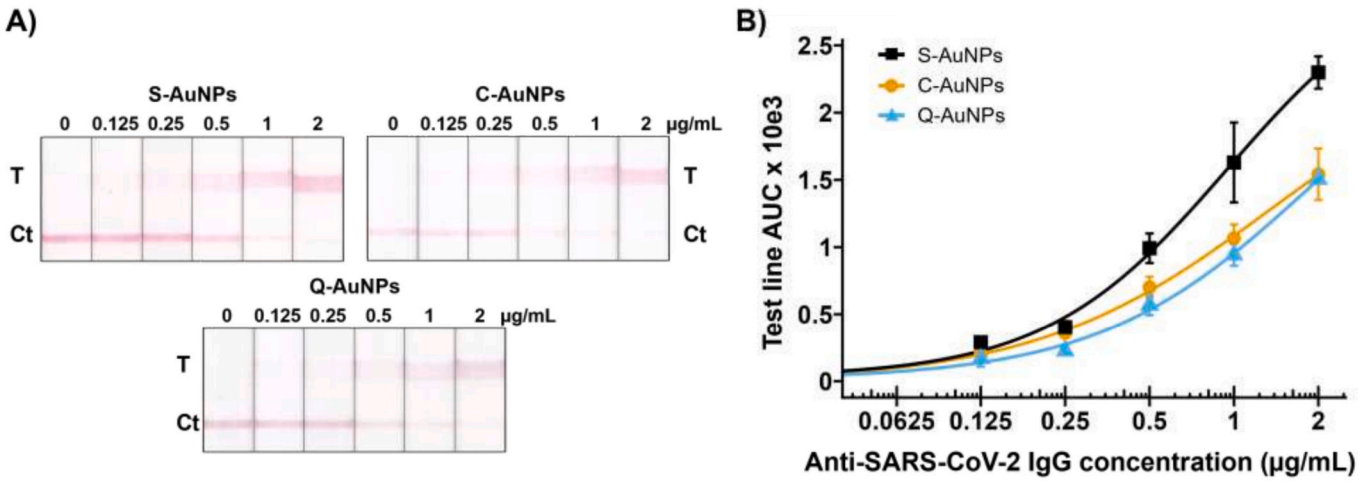

Fig. 4. Quantitative study of LFIA strips with different gold nanoparticle (AuNP) morphology. A) Test strips images after detection of anti-SARS-CoV-2 antibodies spiked in plasma at 0, 0.125, 0.25, 0.5, 1, and 2 µg/mL. B) Test line area under the peak (AUP) measurements as a function of anti-SARS-CoV-2 antibodies tested on LFIAs using spherical (*S*)-AuNPs (black) $R^2 = 0.997$; commercial (C)-AuNPs (yellow) $R^2 = 0.999$; and quasi-spherical (Q)-AuNPs (blue) $R^2 = 0.997$. The data represent mean ± SD (error bars, n = 3). (For interpretation of the references to colour in this figure legend, the reader is referred to the web version of this article.)

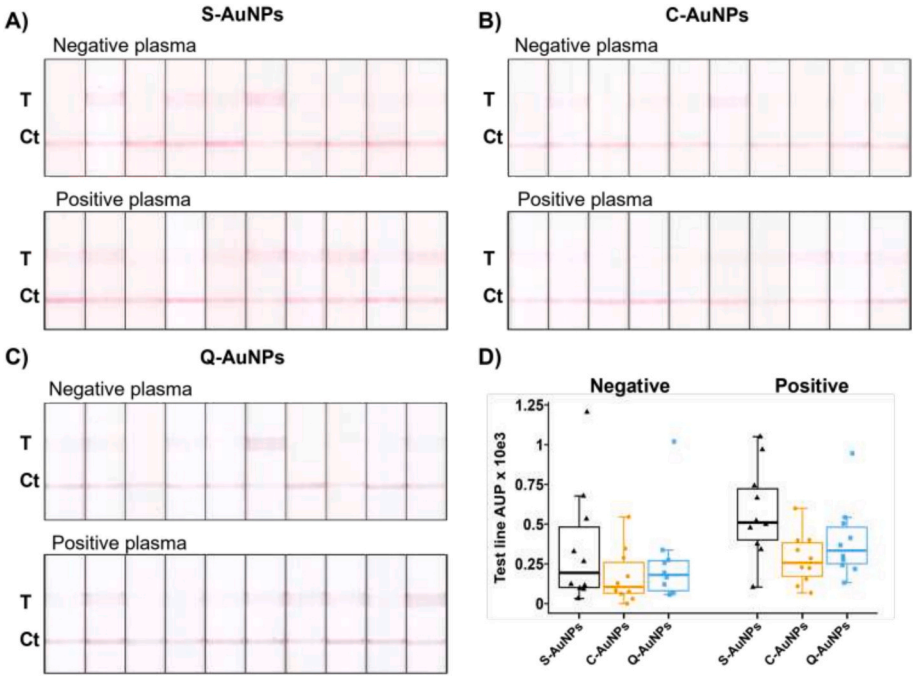

Fig. 5. Representative images of LFIAs using A) spherical (S), B) commercial (C) and C) quasi-spherical (Q) gold nanoparticles (AuNPs) showing negative samples (top) and positive samples (bottom). D) Boxplot of human plasma samples tested with the LFIAs according to AuNP morphology showing C-AuNPs (yellow), S-AuNPs (white), and Q-AuNPs (blue). The data represents median test line area under the peak (AUP) ± 95 % CI (error bars, n = 3). (For interpretation of the references to colour in this figure legend, the reader is referred to the web version of this article.)

Varying levels of specificity and sensitivity were observed from all AuNPs morphologies (Table 2), the highest sensitivity was observed from S-AuNPs (90 %) and C-AuNPs presented the highest specificity (60 %). It is possible that higher sensitivity from S-AuNPs, as observed in the lower LOD (56 ng/mL), contributed to the increase in false positives in the assays and therefore lower specificity rating. However, Q-AuNPs demonstrated equally high sensitivity (90 %) and lower specificity (40 %) to S-AuNPs, even though their LOD was the highest (107 ng/mL). It is possible that the lower sphericity and monodispersity seen in Q-AuNPs contributed to the slightly lower specificity compared to S-AuNPs.

Although LFIAs only had 50 % specificity, the mean intensities of negative and positive samples noticeably increased for all AuNP

Table 2
Detection of anti-SARS-CoV-2 IgG in human plasma by LFIAs of different AuNP morphologies ($n = 3$).

	S-AuNPs	C-AuNPs	Q-AuNPs
FP	5	4	6
FN	1	2	1
TP	9	8	9
TN	5	6	4
Specificity (%)	50	60	40
Sensitivity (%)	90	80	90

FP: False positive; FN: False negative; TP: true positive; TN: true negative. Sensitivity = TP/(TP + FN); specificity = TN/(TN + FP).

morphologies (Fig. 5D). The greatest AUP median difference was observed for S-AuNPs (227.6), followed by Q-AuNPs (137.8), and C-AuNPs (107.3). Large error bars were observed for S-AuNPs in Fig. 5D, this is likely the result of donor-donor variability as we used plasma donations of varying levels of antibodies as biological replicas. Some of which fall at the extreme ends of the level gauges with low and high titers. Higher sensitivities, as with S-AuNPs, will increase the contrast between the two extremes and result in larger error bars.

Since all sensitivity and specificity ratings were similar, with only 10 positive and negative samples tested, the determination of the optimal AuNP morphology using complex clinical plasma samples still requires further investigation.

3.6. Semi-quantitative LFIA pattern design

The S-AuNPs with higher sensitivity were used as labels in a barcode-LFIA to semi-quantitatively detect anti-SARS-CoV-2 antibodies levels in plasma as low, medium, and high. The three T lines develop sequentially with increasing antibody levels (Fig. 6A). The following patterns were explored: pattern 1- three T lines consisting of the same concentration of

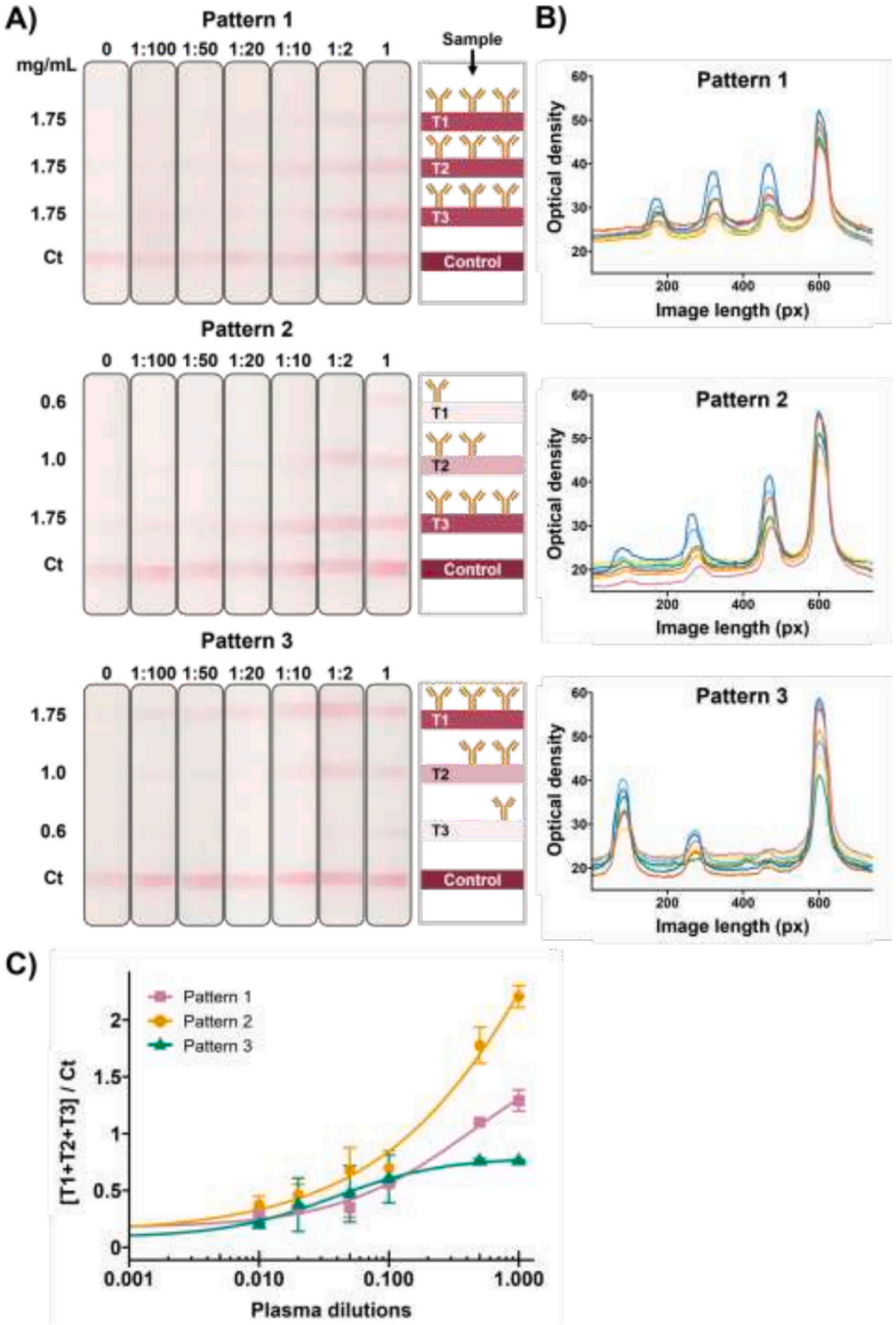

Fig. 6. Pattern design for semi-quantitative LFIA using spherical gold nanoparticles (S-AuNPs). A) Scanned images of LFIAs with 3 patterns: Pattern 1 with 3 test lines coated with the same concentration of capture antibody, pattern 2 with increasing concentration of capture antibody, and pattern 3 with decreasing concentration of capture antibody. B) Optical density plots of test strips at various dilutions of positive anti-SARS-CoV-2 plasma (1–1/100). C) 4PL nonlinear function fit of [T1 + T2 + T3] / Ct values versus plasma dilutions comparing pattern 1 (pink squares), pattern 2 (yellow circles), and pattern 3 (green triangles). The data represents mean test line area under the peak (AUP) ± SD (error bars, n = 3). (For interpretation of the references to colour in this figure legend, the reader is referred to the web version of this article.)

capture antibodies (1.75 mg/mL); pattern 2- increasing concentration of capture antibodies (T1(2) = 0.6, T2(2) = 1.0, T3(2) = 1.75 mg/mL); and pattern 3- decreasing concentration of capture antibodies (T1(3) = 1.75, T2(3) = 1.0, T3(3) = 0.6 mg/mL). The Ct line was coated with a higher concentration of control antibody (0.8 mg/mL) to account for the severe loss in intensity seen in Fig. 4.

Each LFIA pattern was evaluated with a series of dilutions of a clinical plasma sample with high level of anti-SARS-CoV-2 antibodies as previously determined through ELISA [49,54]. Antibody titers were defined according to standardized criteria established previously [54]. A high antibody titer is defined as the level at which antibodies remain detectable at dilutions of 1:80 and higher, medium titers correspond to antibody levels detectable between 1:41 and 1:79 dilutions, and a low titer is detectable only up to a 1:40 dilution [49,54]. This means there could be medium samples with levels closer to the thresholds of adjacent titers. The plasma sample classified as high titer was serially diluted (1:100, 1:50, 1:20, 1:10, 1:2, 1) to correspond with the dilution ranges up to 1:80 used in ELISA-based grading.

The strips were scanned and analyzed with MATLAB to obtain the ODs of T and Ct lines, where the AUP was used for all subsequent calculations (Fig. 6B). Fig. 6C represents the 4PL nonlinear fit of the sum of T lines AUP divided by the Ct line AUP ([T1 + T2 + T3] / C) according to plasma dilutions, with R^2 values of 0.990, 0.990, and 0.991; and LODs of 1/303, 1/65, and 1/18 for patterns 1, 2, and 3, respectively. Decreasing the sample concentration resulted in all T lines fading simultaneously in pattern 1. In comparison, in patterns 2 and 3 the decrease in sample concentration caused the complete and sequential fading of T lines, thus demonstrating higher contrast between dilutions. Although pattern 1 demonstrated better quantitative performance with a lower LOD, pattern 2 was selected for the next study with clinical COVID-19 plasma samples as it showed higher contrast between dilutions with a strong fit with the 4PL nonlinear model.

3.7. Semi-quantitative LFIA with clinical COVID-19 samples

Ten COVID-19 plasma samples were tested with pattern 2 barcode-LFIA to evaluate its performance in differentiating between low, medium, and high samples (Fig. 7A). Since it is unlikely that the barcode-LFIA will improve the rate of false positives observed above, only samples that were positive for anti-SARS-CoV-2 antibodies were tested. The current proof-of-concept still requires further optimization to the bioreceptors and buffers to improve specificity. Fig. 7B shows the scanned test strips, and [T1 + T2 + T3] / Ct values were plotted in Fig. 7C, with a colour gradient representing the contribution of each T line (T1 = red, T2 = orange, T3 = yellow). The contribution of T lines as a proportion of the intensity of the Ct line was used to designate the antibody levels as low (L), medium (M), or high (H). T lines were considered positive at intensity above 15 % of the control line (T / Ct ≥ 0.15). This was evaluated from the AUP of the serial dilutions of a positive control sample from the previous study (Fig. 6), where the AUP of T lines that could not be visually detected was less than 15 % of the control AUP.

The number of positive T lines represented the final level of antibodies, for example, a score of 1 with 1 positive T line meant that the sample's antibody level was low. All samples were assigned numeric scores of 1, 2 or 3 representing L-M-H levels. Antibody levels had been pre-measured using ELISA and classified according to the last detectable dilution as L = ≤ 1:40, M = 1:41–1:79, and H = ≥1:80 [49]. After testing with the barcode-LFIA, another 1, 2 or 3 value was given to represent the LFIA result, and both scores from ELISA and LFIA were used to plot the confusion matrix in Fig. 7D. Although only 50 % of samples were perfectly aligned with the validation method, 90 % of the results fell within ±1 category of the reference values (Fig. 7D). Given that antibody titers are categorized according to the highest sample dilution where the antibody was last detected, any given sample could fall at either the higher or lower end of the dilution range. Although clear

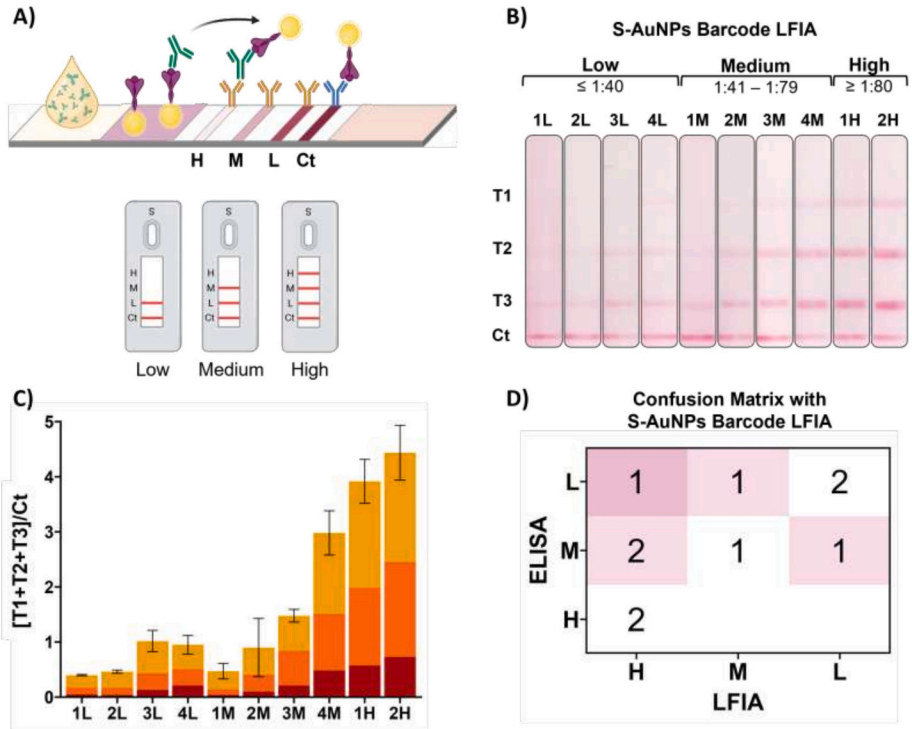

Fig. 7. Detection of anti-SARS-CoV-2 antibody levels using the barcode-style lateral flow immunoassay (LFIA). A) Schematic of the barcode-LFIA for the semi-quantitative detection of anti-SARS-CoV-2 antibodies as low (L), medium (M), or high (H). B) Scanned images of the barcode-LFIA with spherical gold nanoparticles (S-AuNPs) showing positive samples of varying levels of anti-SARS-CoV-2 antibody titers with sample code. C) [T1 + T2 + T3] / Ct values of test strips for each plasma sample, where colors indicate contribution of each T line as yellow = T1, orange = T2, and red = T3. The data represents mean test line area under the peak (AUP) ± SD (error bars, n = 3). D) Confusion matrix of correlation between ELISA and barcode-style LFIA results, with the labels representing the sample count. (For interpretation of the references to colour in this figure legend, the reader is referred to the web version of this article.)

distinctions between titers were previously observed with the positive control (Fig. 5), in reality, using clinical samples will introduce variability that can obscure the differences between adjacent categories (L-M and M-H).

As it was only possible to obtain access to titer classifications – and not specific antibody titers – for all samples, there is a possibility that these samples fall at the upper or lower ends of their given category. However, the actual degree of deviation is unknown and warrants further investigation. Nevertheless, most LFIA results showed antibody titers that were only one level away from the reference values. These results indicate that the barcode-LFIA holds promise as a semi-quantitative POC serological tool, however, it requires further optimization to fine-tune the resolution between categories and increase the correlation with reference methods.

4. Conclusion

This study presents a proof-of-concept for the development of a novel barcode-LFIA for the semi-quantitative detection of antibody levels in human plasma. Three AuNPs morphologies and LFIA patterns were assessed for increased sensitivity and performance. It was shown that highly spherical citrate-based AuNPs (S-AuNPs), synthesized with a simple and reproducible seeded growth method, have higher sphericity and monodispersity than C-AuNPs and typical Q-AuNPs synthesized using the common Turkevich method as the LOD for S-AuNPs was 2-fold lower than C-AuNPs and Q-AuNPs. Tests with real-life COVID-19 plasma samples showed that all AuNPs were similar in specificity and sensitivity (~80 %, ~50 %), but a greater difference between the intensity of negative and positive samples was observed for S-AuNPs. The barcode-LFIA constructed with S-AuNPs performed best with the 3 test lines consisting of the same concentration of capture antibody. This LFIA was used to semi-quantify 10 human plasma samples of different anti-SARS-CoV-2 antibody levels.

As a proof-of-concept, the present LFIA requires further optimization to improve specificity and sensitivity metrics as well as stringent validation with a larger sample size and an evaluation of the long-term shelf stability. Even though only 50 % of samples were in accordance with the validation method, 90 % of the samples of the results fell within ±1 category of the reference values. This barcode-LFIA therefore showed initial promise as a quick, easy, and equipment-free tool for serological testing in POC settings.

CRediT authorship contribution statement

Laura M. Rey Gomez: Writing – review & editing, Writing – original draft, Visualization, Validation, Project administration, Methodology, Investigation, Formal analysis, Data curation, Conceptualization. **Rena Hirani:** Writing – review & editing, Supervision, Methodology, Conceptualization. **David W. Inglis:** Writing – review & editing, Supervision, Methodology. **Andrew Care:** Writing – review & editing, Supervision, Methodology. **Yuling Wang:** Writing – review & editing, Supervision, Resources, Methodology, Conceptualization.

Author statement

All authors approve of the revised manuscript for publication.

Declaration of competing interest

The authors declare that they have no known competing financial interests or personal relationships that could have appeared to influence the work reported in this paper.

Acknowledgements

The authors acknowledge the funding support from the government funded Research Training Program (RTP) Scholarship for the Doctor of Philosophy in Natural Sciences Program at Macquarie University, the support from the Alexander Steele Young Memorial Lions Foundation through the Alex Young Lions Scholarship, as well as the Macquarie University Microscopy Unit for access to its instrumentation and staff. Australian governments fund Australian Red Cross Lifeblood to provide blood, blood products and services to the Australian community. Fig. 1 was partially created in BioRender. Rey Gomez, L.M. (2025) [https://BioRender.com/61jjo8h].

Appendix A. Supplementary data

Supplementary data to this article can be found online at https://doi.org/10.1016/j.sbsr.2025.100900.

Data availability

The data supporting this article have been included as part of the Supplementary Information.

References

[1] A.M. Brady, E. El-Badry, E. Padron-Regalado, N.A. Escudero González, et al., Serosurveillance for measles and rubella, Vaccines 12 (7) (2024) 816, https://doi.org/10.3390/vaccines12070816.
[2] X. Chen, Z. Chen, A.S. Azman, X. Deng, et al., Serological evidence of human infection with Sars-Cov-2: a systematic review and meta-analysis, Lancet Glob. Health 9 (5) (2021) e598–e609, https://doi.org/10.1016/S2214-109X(21)00026-7.
[3] S. Ghosh, A. Kotwal, K. Pandya, A.K. Yadav, Sero-surveillance of Sars-Cov2 infection among health-care workers: a protocol, Med. J. Dr. D.Y. Patil Vidyapeeth. 14 (2) (2021) 123, https://doi.org/10.4103/mjdrdypu.mjdrdypu_529_20.
[4] N. Kohmer, S. Westhaus, C. Rühl, S. Ciesek, et al., Clinical performance of different Sars-Cov-2 igg antibody tests, J. Med. Virol. 92 (10) (2020) 2243–2247, https://doi.org/10.1002/jmv.26145.
[5] A. Menezes, S.L. Razafimahatratra, O. Wariri, A.L. Graham, et al., Strengthening serological studies: the need for greater geographical diversity, biobanking, and data-accessibility, Trends Microbiol. 0 (0) (2025), https://doi.org/10.1016/j.tim.2024.12.006.
[6] S. Chen, L. Meng, L. Wang, X. Huang, et al., Sers-based lateral flow immunoassay for sensitive and simultaneous detection of anti-Sars-Cov-2 Igm and igg antibodies by using gap-enhanced Raman Nanotags, Sensors Actuators B Chem. 348 (2021) 130706, https://doi.org/10.1016/j.snb.2021.130706.
[7] S. Srivastav, A. Dankov, M. Adanalic, R. Grzeschik, et al., Rapid and sensitive Sers-based lateral flow test for Sars-Cov2-Specific Igm/Igg antibodies, Anal. Chem. 93 (36) (2021) 12391–12399, https://doi.org/10.1021/acs.analchem.1c02305.
[8] X. Duan, Y. Shi, X. Zhang, X. Ge, et al., Dual-detection fluorescent Immunochromatographic assay for quantitative detection of Sars-Cov-2 spike Rbd-Ace2 blocking neutralizing antibody, Biosens. Bioelectron. 199 (2022) 113883, https://doi.org/10.1016/j.bios.2021.113883.
[9] M. Kumar Dey, M. Iftesum, R. Devireddy, M. Ranjan Gartia, New technologies and reagents in lateral flow assay (Lfa) designs for enhancing accuracy and sensitivity, Anal. Methods 15 (35) (2023) 4351–4376, https://doi.org/10.1039/D3AY00844D.
[10] D.V. Baker, J. Bernal-Escalante, C. Traaseth, Y. Wang, et al., Smartphones as a platform for molecular analysis: concepts, methods, devices and future potential, Lab Chip 25 (5) (2025) 884–955, https://doi.org/10.1039/D4LC00966E.
[11] C. Fang, Z. Chen, L. Li, J. Xia, Barcode lateral flow Immunochromatographic strip for prostate acid phosphatase determination, J. Pharm. Biomed. Anal. 56 (5) (2011) 1035–1040, https://doi.org/10.1016/j.jpba.2011.08.008.
[12] H.-Y. Yin, P.-T. Chu, W.-C. Tsai, H.-W. Wen, Development of a barcode-style lateral flow immunoassay for the rapid semi-quantification of gliadin in foods, Food Chem. 192 (2016) 934–942, https://doi.org/10.1016/j.foodchem.2015.06.112.
[13] K. Misawa, T. Yamamoto, Y. Hiruta, H. Yamazaki, et al., Text-displaying Semiquantitative competitive lateral flow immunoassay relying on inkjet-printed patterns, ACS Sensors 5 (7) (2020) 2076–2085, https://doi.org/10.1021/acssensors.0c00637.
[14] D. Zhang, P. Li, W. Liu, L. Zhao, et al., Development of a detector-free Semiquantitative Immunochromatographic assay with major aflatoxins as target Analytes, Sensors Actuators B Chem. 185 (2013) 432–437, https://doi.org/10.1016/j.snb.2013.05.034.
[15] L.A. Contreras Alvarez, M.D. Lazo Jara, F.V. Campos, J.P. de Oliveira, et al., Barcode-style lateral flow Immunochromatographic strip for the semi-quantitative detection of Ochratoxin a in coffee samples, Food Addit. Contam. Part A. 41 (4) (2024) 424–437, https://doi.org/10.1080/19440049.2024.2313115.
[16] G. Yang, J. Li, S. Zhang, H. Ouyang, et al., A flexible gradient lateral flow Immunochromatographic assay for qualitative, semi-quantitative, and quantitative determination of serum amyloid a, J. Immunol. Methods 523 (2023) 113574, https://doi.org/10.1016/j.jim.2023.113574.

[17] K.V. Serebrennikova, J.V. Samsonova, A.P. Osipov, A semi-quantitative rapid multi-range gradient lateral flow immunoassay for Procalcitonin, Microchim. Acta 186 (7) (2019) 423, https://doi.org/10.1007/s00604-019-3550-2.
[18] V.G. Panferov, I.V. Safenkova, A.V. Zherdev, B.B. Dzantiev, Setting up the cut-off level of a sensitive barcode lateral flow assay with magnetic nanoparticles, Talanta 164 (2017) 69–76, https://doi.org/10.1016/j.talanta.2016.11.025.
[19] W. Leung, C.P. Chan, T.H. Rainer, M. Ip, et al., Infectcheck Crp barcode-style lateral flow assay for semi-quantitative detection of C-reactive protein in distinguishing between bacterial and viral infections, J. Immunol. Methods 336 (1) (2008) 30–36, https://doi.org/10.1016/j.jim.2008.03.009.
[20] H. Park, C. Yu, L.-A. Pirofski, H. Yoon, et al., Association between Covid-19 convalescent plasma antibody levels and Covid-19 outcomes stratified by clinical status at presentation, BMC Infect. Dis. 24 (1) (2024) 639, https://doi.org/10.1186/s12879-024-09529-0.
[21] M. Franchini, M. Cruciani, A. Casadevall, M.J. Joyner, et al., Safety of Covid-19 convalescent plasma: a definitive systematic review and meta-analysis of randomized controlled trials, Transfusion 64 (2) (2024) 388–399, https://doi.org/10.1111/trf.17701.
[22] E.M. Bloch, D. Focosi, S. Shoham, J. Senefeld, et al., Guidance on the use of convalescent plasma to treat immunocompromised patients with coronavirus disease 2019, Clin. Infect. Dis. 76 (11) (2023) 2018–2024, https://doi.org/10.1093/cid/ciad066.
[23] J.J. Deeks, J. Dinnes, Y. Takwoingi, C. Davenport, et al., Antibody tests for identification of current and past infection with Sars-Cov-2, Cochrane Database Syst. Rev. (6) (2020), https://doi.org/10.1002/14651858.CD013652.
[24] M. Lisboa Bastos, G. Tavaziva, S.K. Abidi, J.R. Campbell, et al., Diagnostic accuracy of serological tests for Covid-19: systematic review and Meta-analysis, BMJ 370 (2020) m2516, https://doi.org/10.1136/bmj.m2516.
[25] L. Zhan, S.-Z. Guo, F. Song, Y. Gong, et al., The role of nanoparticle Design in Determining Analytical Performance of lateral flow immunoassays, Nano Lett. 17 (12) (2017) 7207–7212, https://doi.org/10.1021/acs.nanolett.7b02302.
[26] N.A. Byzova, A.V. Zherdev, B.N. Khlebtsov, A.M. Burov, et al., Advantages of highly spherical gold nanoparticles as labels for lateral flow immunoassay, Sensors 20 (12) (2020) 3608, https://doi.org/10.3390/s20123608.
[27] G. Ruiz, K. Tripathi, S. Okyem, J.D. Driskell, Ph impacts the orientation of antibody adsorbed onto gold nanoparticles, Bioconjug. Chem. 30 (4) (2019) 1182–1191, https://doi.org/10.1021/acs.bioconjchem.9b00123.
[28] Z.-Y. Lu, Y.-H. Chan, The importance of antibody orientation for enhancing sensitivity and selectivity in lateral flow immunoassays, Sens. Diagn. 3 (10) (2024) 1613–1634, https://doi.org/10.1039/D4SD00206G.
[29] J. Zhang, F. Chai, J.A. Li, S. Wang, et al., Weakly ionized gold nanoparticles amplify immunoassays for ultrasensitive point-of-care sensors, Sci. Adv. 10 (28) (2024) eadn5698, https://doi.org/10.1126/sciadv.adn5698.
[30] P. Zhang, Y. Li, D. Wang, H. Xia, High–yield production of uniform gold nanoparticles with sizes from 31 to 577 Nm via one-pot seeded growth and size-dependent sers property, Part. Part. Syst. Charact. 33 (12) (2016) 924–932, https://doi.org/10.1002/ppsc.201600188.
[31] Merck Life Science Pty Ltd, Gold Nanoparticles 50 Nm Diameter, Od 1, Stabilized Suspension in 0.1 Mm Pbs, Reactant Free Aunp. https://www.sigmaaldrich.com/AU/en/product/aldrich/753645, 2025 (Accessed 01/30/2025).
[32] J. Turkevich, P.C. Stevenson, J. Hillier, A study of the nucleation and growth processes in the synthesis of colloidal gold, Discuss. Faraday Soc. 11 (0) (1951) 55–75, https://doi.org/10.1039/DF9511100055.
[33] C. Huang, T. Wen, F.-J. Shi, X.-Y. Zeng, et al., Rapid detection of Igm antibodies against the Sars-Cov-2 virus via colloidal gold nanoparticle-based lateral-flow assay, ACS Omega 5 (21) (2020) 12550–12556, https://doi.org/10.1021/acsomega.0c01554.
[34] A. Chamorro-Garcia, A. de la Escosura-Muñiz, M. Espinoza-Castañeda, C. J. Rodriguez-Hernandez, et al., Detection of parathyroid hormone-like hormone in Cancer cell cultures by gold nanoparticle-based lateral flow immunoassays, Nanomedicine 12 (1) (2016) 53–61, https://doi.org/10.1016/j.nano.2015.09.012.
[35] A. Ambrosi, M.T. Castañeda, A.J. Killard, M.R. Smyth, et al., Double-codified gold Nanolabels for enhanced Immunoanalysis, Anal. Chem. 79 (14) (2007) 5232–5240, https://doi.org/10.1021/ac070357m.
[36] C.A. Schneider, W.S. Rasband, K.W. Eliceiri, Nih image to Imagej: 25 years of image analysis, Nat. Methods 9 (7) (2012) 671–675, https://doi.org/10.1038/nmeth.2089.
[37] K. Saxena, B. Toley, Streamlining Lateral Flow Assay (Lfa) Data Analysis: A Matlab® Live Script for Integrated Batch Image Processing and Limit of Detection Determination, 2024, https://doi.org/10.26434/chemrxiv-2024-wr3kj.
[38] M.S. Woolf, L.M. Dignan, A.T. Scott, J.P. Landers, Digital postprocessing and image segmentation for objective analysis of colorimetric reactions, Nat. Protoc. 16 (1) (2021) 218–238, https://doi.org/10.1038/s41596-020-00413-0.
[39] R: A Language and Environment for Statistical Computing; R Foundation for Statistical Computing: Vienna, Austria, 2025 (accessed).
[40] Rstudio: Integrated Development for R, RStudio, PBC, Boston, MA, 2020 (accessed).
[41] D.A. Armbruster, T. Pry, Limit of blank, limit of detection and limit of quantitation. The clinical biochemist, Reviews 29 (Suppl. 1) (2008) S49–S52.
[42] W. Tai, L. He, X. Zhang, J. Pu, et al., Characterization of the receptor-binding domain (Rbd) of 2019 novel coronavirus: implication for development of Rbd protein as a viral attachment inhibitor and vaccine, Cell. Mol. Immunol. 17 (6) (2020) 613–620, https://doi.org/10.1038/s41423-020-0400-4.
[43] L.L. Luchsinger, B.P. Ransegnola, D.K. Jin, F. Muecksch, et al., Serological assays estimate highly variable Sars-Cov-2 neutralizing antibody activity in recovered Covid-19 patients, J. Clin. Microbiol. 58 (12) (2020) e02005-02020, https://doi.org/10.1128/JCM.02005-20.
[44] W. Haiss, N.T.K. Thanh, J. Aveyard, D.G. Fernig, Determination of size and concentration of gold nanoparticles from Uv−Vis spectra, Anal. Chem. 79 (11) (2007) 4215–4221, https://doi.org/10.1021/ac0702084.
[45] B.N. Khlebtsov, N.G. Khlebtsov, On the measurement of gold nanoparticle sizes by the dynamic light scattering method, Colloid J. 73 (1) (2011) 118–127, https://doi.org/10.1134/S1061933X11010078.
[46] F. Krebs, C. Scheller, K. Grove-Heike, L. Pohl, et al., Isoelectric point determination by imaged Cief of commercially available Sars-Cov-2 proteins and the Hace2 receptor, ELECTROPHORESIS 42 (6) (2021) 687–692, https://doi.org/10.1002/elps.202100015.
[47] C. Parolo, A. Sena-Torralba, J.F. Bergua, E. Calucho, et al., Tutorial: design and fabrication of nanoparticle-based lateral-flow immunoassays, Nat. Protoc. 15 (12) (2020) 3788–3816, https://doi.org/10.1038/s41596-020-0357-x.
[48] J.W.A. Findlay, R.F. Dillard, Appropriate calibration curve fitting in ligand binding assays, AAPS J. 9 (2) (2007) E260–E267, https://doi.org/10.1208/aapsj0902029.
[49] R. Hirani, V. Hoad, I.B. Gosbell, D.O. Irving, Absence of correlation between abo Rh(D) blood group and neutralizing antibody titers in Sars-Cov-2 convalescent plasma donors, Transfusion 62 (2) (2022) 292–297, https://doi.org/10.1111/trf.16781.
[50] N. Zhu, D. Zhang, W. Wang, X. Li, et al., A novel coronavirus from patients with pneumonia in China, 2019, N. Engl. J. Med. 382 (8) (2020) 727–733, https://doi.org/10.1056/NEJMoa2001017.
[51] N. Bolstad, D.J. Warren, K. Nustad, Heterophilic antibody interference in immunometric assays, Best Pract. Res. Clin. Endocrinol. Metab. 27 (5) (2013) 647–661, https://doi.org/10.1016/j.beem.2013.05.011.
[52] L. Wauthier, M. Plebani, J. Favresse, Interferences in immunoassays: review and practical algorithm, Clin. Chem. Lab. Med. 60 (6) (2022) 808–820, https://doi.org/10.1515/cclm-2021-1288.
[53] J.F. Emerson, K.K.Y. Lai, Endogenous antibody interferences in immunoassays, Lab. Med. 44 (1) (2013) 69–73, https://doi.org/10.1309/LMMURCFQHKSB5YEC.
[54] G.J. Walker, Z. Naing, A. Ospina Stella, M. Yeang, et al., Sars Coronavirus-2 Microneutralisation and commercial serological assays correlated closely for some but not all enzyme immunoassays, Viruses 13 (2) (2021) 247, https://doi.org/10.3390/v13020247.